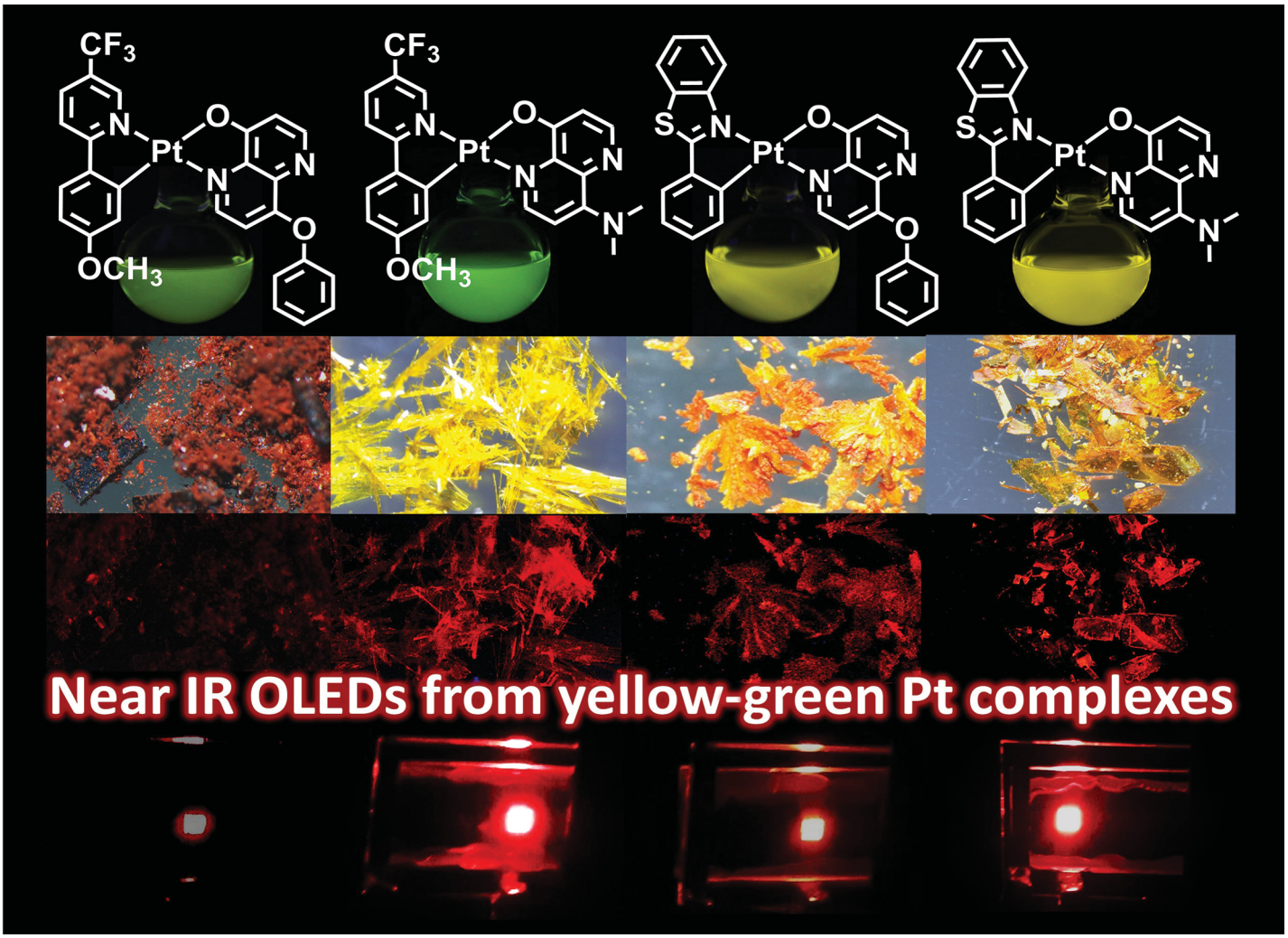

Showcasing research from Professor Chin-Ti Chen's laboratory, Institute of Chemistry, Academia Sinica, Taipei, Taiwan.

Photoluminescence and electroluminescence characterization of high-performance near-infrared emitters based on 1,5-naphthyridin-4-ol-containing heteroleptic platinum(II) complexes

High efficiency (maximum EQE 10.1%) near IR electroluminescence (λ^{EL}_{max} 704–774 nm) has been achieved with platinum complexes with greenish yellow photoluminescence (λ^{EL}_{max} 523–546 nm) in diluted solution. Through our study, it is demonstrated that the high EQE of near IR electroluminescence is due to an appropriate molecular alignment of the platinum complex, which enhances the light outcoupling efficiency of near IR OLEDs up to 32%, ~1.6 times higher than ~20% of most conventional OLEDs.

As featured in:

See Chin-Ti Chen *et al.*, *Mater. Adv.*, 2021, **2**, 3589.

ROYAL SOCIETY OF CHEMISTRY

rsc.li/materials-advances

Registered charity number: 207890

Materials Advances

ROYAL SOCIETY OF CHEMISTRY

PAPER

View Article Online
View Journal | View Issue

Cite this: *Mater. Adv.*, 2021, 2, 3589

Photoluminescence and electroluminescence characterization of high-performance near-infrared emitters based on 1,5-naphthyridin-4-ol-containing heteroleptic platinum(II) complexes†

Hagos Tesfay Kidanu, [abc] Jian Haur Lee[abc] and Chin-Ti Chen *[a]

Four 1,5-naphthyridin-4-ol-containing platinum complexes, **AtFOND**, **AtFNND**, **PBSOND**, and **PBSNND**, have been synthesized and characterized for their photoluminescence (PL) and electroluminescence (EL) properties. In addition to supporting the aggregate/excimer formation of the four platinum complexes in the solid state, the absorption and emission spectra of the solution, dopant thin film, and solid state suggest that the metal–metal-to-ligand charge transfer (MMLCT) is the main reason for the very long emission wavelengths of λ_{max} 770 and 774 nm for PL and EL of **AtFOND**, respectively. The MMLCT is inferable from the single-crystal X-ray structure, namely, the Pt–Pt contacts which are short (3.39 and 3.88 Å) and almost normal to the molecular planes of **AtFOND**. The solid-state PL quantum yield (PLQY) has been determined to be 9%, 58%, 53%, and 33% for **AtFOND**, **AtFNND**, **PBSOND**, and **PBSNND**, respectively. Although the four platinum complexes show green to yellow (λ_{max}^{PL} 523–546 nm) PL in diluted solution, all non-dopant OLEDs with a thin emissive layer (2 nm) based on **AtFOND**, **AtFNND**, **PBSOND**, and **PBSNND** display NIR (λ_{max}^{EL} 704–774 nm) EL with EQE values of 1.8%, 6.5%, 4.0%, and 10.1%, respectively. The relatively high EQE (10.1%) of the **PBSNND** NIR OLED can be ascribed to the molecular alignment in the thin film that enhances the light outcoupling of the devices. Together with the single-crystal X-ray structure, the 2D-GIWAXS study provides convincing evidence for the advantageous molecular alignment of **PBSNND**.

Received 16th February 2021,
Accepted 6th April 2021

DOI: 10.1039/d1ma00141h

rsc.li/materials-advances

Introduction

Different from displays and lighting, essentially invisible near-infrared (NIR) emitters find their niche applications in fibre optic telecommunication, night vision technologies, wound healing, and bioimaging and as chemosensing materials.[1–5] For practical reasons, NIR organic light-emitting diodes (OLEDs) attract increasing research efforts due to their high electroluminescence (EL) efficiency.[6–8] Most NIR emitters exhibit low EL efficiency, except for Pt complexes.[9–11] Complexes, having a square planar molecular structure, are known to form excimers emitting long wavelengths in the deep red or NIR region (λ_{max} > 700 nm).[12–14] Due to the exciton self-trapping of excimers,[15] the detrimental triplet–triplet annihilation, which is usually prevalent for a heavy metal-based phosphorescence emitter in a non-dopant thin film, is alleviated.[16,17] NIR emissions from the excimer of Pt complexes have the advantage of high EL efficiency over other NIR emitters. A high external quantum efficiency (EQE) of >10%, even as high as >20%, has been reported in recent years.[13,18]

Herein, we report four NIR emitting heteroleptic Pt complexes based on two 1,5-naphthyridin-4-ol (**ND**) derivatives, 4-hydroxy-8-phenoxy-1,5-naphthyridine (**OPhNDH**) and 4-hydroxy-8-dimethylamino-1,5-naphthyridine (**dmaNDH**) (Scheme 1), the Pt complexes of which have been demonstrated by us for high-performance hybrid white OLEDs before.[19–21] By incorporating the second ligand, either 2-(4-methoxyphenyl)-5-(trifluoromethyl)pyridine (**AtF**) or 2-phenylbenzo[*d*]thiazole (**PBS**), the Pt complexes of **AtFOND**, **AtFNND**, **PBSOND**, and **PBSNND** (Scheme 1) have been synthesized and characterized. We have studied their photoluminescence (PL) and EL in detail. The voltage-independent NIR with λ_{max}^{EL} of 774, 744, 726, and 702 nm has been observed for **AtFOND**, **AtFNND**, **PBSOND**, and **PBSNND**, respectively, among which an EQE as high as 10.1% has been achieved for **PBSNND** NIR OLEDs. Considering its moderate solid-state photoluminescence quantum yield (PLQY) of

[a] *Institute of Chemistry, Academia Sinica, Taipei 11529, Taiwan, Republic of China. E-mail: chintchen@gate.sinica.edu.tw; Fax: +886 2 27831237; Tel: +886 2 55728542*
[b] *Sustainable Chemical Science and Technology (SCST), Taiwan International Graduate Program (TIGP), Academia Sinica, Taipei 11529, Taiwan, Republic of China*
[c] *Department of Applied Chemistry, National Yang Ming Chiao Tung University, Hsinchu 30050, Taiwan, Republic of China*

† Electronic supplementary information (ESI) available: NMR and MASS spectra, decay profile of the PL, molecular interaction in the crystal, theoretical studies, voltage dependent current density, Q_z of 1D-GIWAXS, and CCDC 2009562, 2009563 and 2009796. For ESI and crystallographic data in CIF or other electronic format see DOI: 10.1039/d1ma00141h

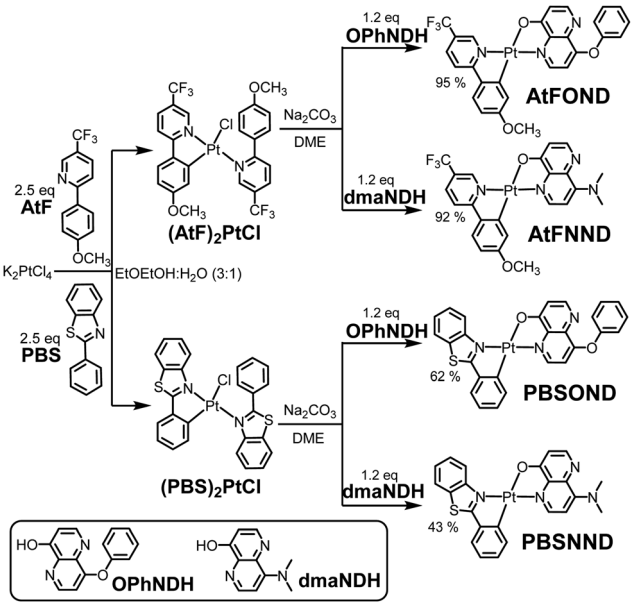

Scheme 1 Synthetic route for **AtFOND**, **AtFNND**, **PBSOND**, and **PBSNND**. The chemical structures of **OPhNDH** and **dmaNDH** are depicted.

~32%, such an EQE is quite unusual. Through the study reported here, we have found that the unusual EQE is due to the enhanced light outcoupling of OLEDs, which was verified by 2D-GIWAXS and single-crystal X-ray crystallography.

Results and discussion

Molecular design and synthesis

The synthesis of the new platinum complexes follows the previous protocol (Scheme 1).[19–21] However, instead of the common method *via* the Pt μ-dichloro-bridged dimer, the four heteroleptic Pt-complexes reported here were prepared through the corresponding monometallic Pt-complex, **$(AtF)_2PtCl$** or **$(PBS)_2PtCl$**. Compared with Pt μ-dichloro-bridged dimer counterparts, monometallic Pt-complexes have a more reasonable solubility, enabling the purification by column chromatography. Purer intermediate monometallic complexes facilitate the final synthesis of the four platinum complexes with much higher yields, although the purity of the two intermediate monometallic complexes isolated from the reaction is already good enough and we just used them directly without further purification. While the synthesis and preparation of ligands, **AtF**, **PBS**, and **dmaNDH**, readily followed a literature procedure,[22,23] **OPhONDH** was synthesized and prepared by a modified procedure[23] with much improved yields (see the Synthesis and materials section for details). The formulation of these complexes was confirmed by NMR spectroscopy, mass spectrometry (see Fig. S1–S14, ESI†), and elemental analyses. Moreover, **AtFOND**, **AtFNND** and **PBSNND** complexes were structurally characterized by single-crystal X-ray crystallography.

X-Ray crystallography

Single crystals of **AtFOND**, **AtFNND**, and **PBSNND** were grown from a dichloromethane/methanol solution. The ORTEP diagrams and some crystal data are shown in Fig. 1 and ref. 24, respectively. All three platinum complexes adopt a distorted square planar geometry and a *trans* conformation between two coordinating nitrogen atoms of **AtF**/**PBS** and **OND**/**NND** ligands. See Table S1 (ESI†) for selected bond distances and bond angles, including those from the DFT calculation and single-crystal X-ray structure. Although sharing a common ligand of **AtF**, the crystal of **AtFOND** and **AtFNND** grows in two different space groups, *i.e.*, *Pbcn* for **AtFOND** and $P\bar{1}$ for **AtFNND**. More importantly, the molecular contact in the crystal of **AtFOND** and **AtFNND** is very different, although both **AtFOND** and **AtFNND** take a pair-wise stacking structure.

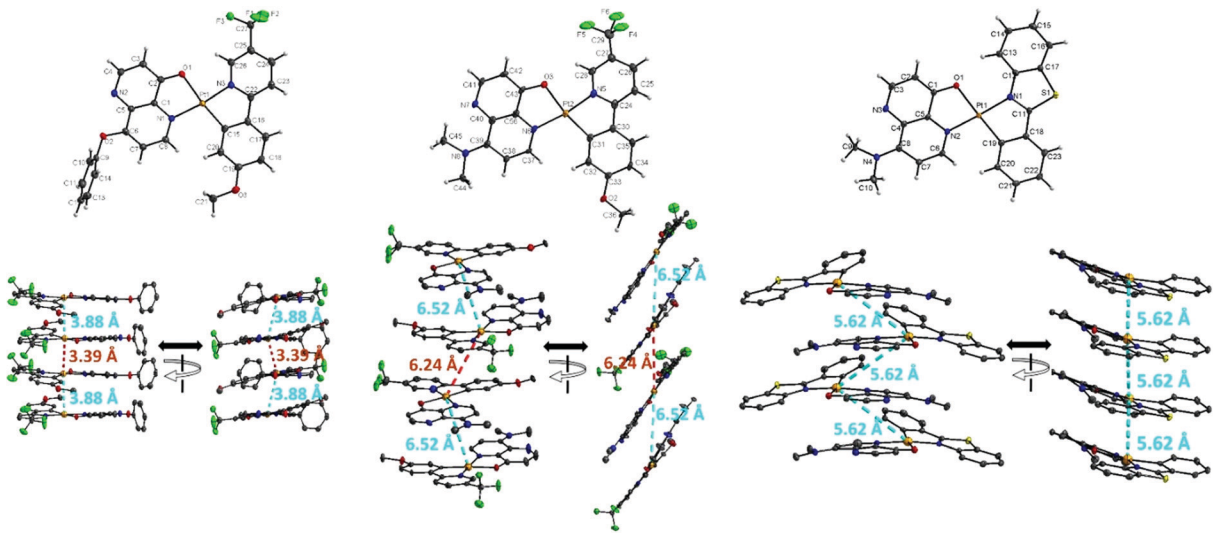

Fig. 1 Top three figures: ORTEP diagram of **AtFOND**, **AtFNND**, and **PBSNND** with thermal ellipsoids shown at about 50% probability level (Pt atoms in the bottom three figures are shown in higher level for clarity). Bottom three figures: molecular stacking diagram (from two viewing angles ~90° difference) with an emphasis on the near-vertical (to the molecular plane) and short contacts (3.39 and 3.88 Å) among Pt atoms of **AtFOND**, but the side-ways sliding and long contacts among Pt atoms of **AtFNND** (6.24, and 6.52 Å) or **PBSNND** (5.62 Å). In the bottom three figures, all hydrogen atoms are removed for clarity.

The crystal of **AtFOND** has short Pt–Pt contacts (3.39 and 3.88 Å), and the Pt–Pt contacts just slightly deviate from the normal direction of the molecular planes. Differently, the crystal of **AtFNND** has long Pt–Pt contacts (5.62 and 6.24 Å), and the Pt–Pt contacts much more deviate from the normal direction of the molecular planes. Essentially, such molecular stacking of **AtFNND** excludes the possible long wavelength absorption from the MMLCT excited state, of which short and near-vertical Pt–Pt contacts are prerequisites. We suggest that this is the reason for the bright yellow colour for the crystal of **AtFNND** but dark brownish red for **AtFOND** (Fig. 2). On the other hand, molecular packing is much tighter for **AtFOND** than **AtFNND** (Fig. 1), which is not favourable for a strong emission in the solid state and consistent with the photoluminescence images of both **AtFOND** and **AtFNND** as crystalline solids (Fig. 2).

Regarding **PBSNND** crystals, long (5.62 Å) and off-vertical Pt–Pt contacts between the molecular planes (Fig. 1) have been observed. Unfortunately, the solid of **PBSOND** obtained from the same single crystal growing process is not suitable for X-ray diffraction. Based on a similar yellowish orange colour for both solids of **PBSOND** and **PBSNND** (Fig. 2), we surmise that the molecular stacking of **PBSOND** has long and off-vertical Pt–Pt contacts, more similar to those of **PBSNND** or **AtFNND** rather than those of **AtFOND**. Based on the dark brownish red colour of **AtFOND** and its longest PL wavelength of 750 nm among the four platinum complexes, we can reasonably infer that **AtFOND** has a MMLCT excited state.

Among the four platinum complexes studied here, **AtFOND** is the only one showing MMLCT-origin absorption and emission in the solid state. By observing the molecular contacts in the single crystal of **AtFOND**, **AtFNND**, and **PBSNND** (Fig. S16, ESI†), no particular short π–π or other contacts but the near-vertical (along the normal direction) and short Pt–Pt contacts (3.39 and 3.88 Å) can be found for **AtFOND** only.

In summary, all four platinum complexes show deep red or NIR PL (Fig. 2 centre row) and EL (see the Electroluminescence properties section) in the solid state, which is very different from the green to yellow emission in solution (Fig. 2 top row). Accordingly, all four platinum complexes form aggregates/excimers in the solid state. From the X-ray crystallography data, only **AtFOND** is possible to have MMLCT in the aggregates/excimers. The solid state (powder and/or crystal) absorption spectra (see Fig. 3 right) of the four platinum complexes show an absorption onset around 650–700 nm for **AtFOND**, which is far longer than ~570 nm of **PBSOND** and **PBSNND**, and ~530 nm of **AtfNND**. Therefore, the solid state absorption spectra further support the existence of the MMLCT excited state of **AtFOND**, which is inferred from the single-crystal X-ray structure.

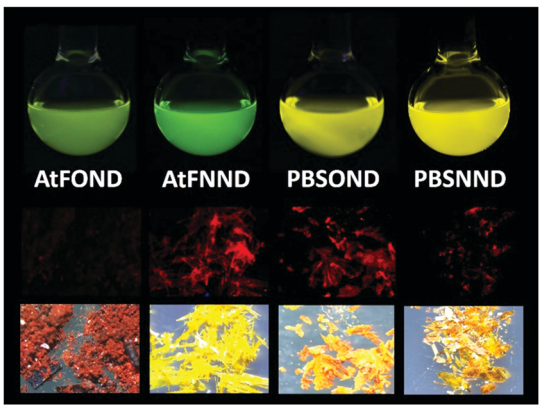

Fig. 2 Solution and solid images of **AtFOND**, **AtFNND**, **PBSOND**, and **PBSNND** (from the left to right). Top row: in a degassed dilute dichloromethane solution of 1×10^{-5} M. Crystals or non-crystalline powders obtained from a solution process of a single crystal grown under 365 nm UV (centre row) and under ambient conditions (bottom row).

UV-vis absorption spectroscopic analysis

The solution and solid-state UV-vis absorption spectra of the four platinum complexes are shown in Fig. 3, and the corresponding data are summarized in Table 1.

These platinum complexes display two regions of absorbance, approximately 280–375 nm and 375–475 nm. The more intense short wavelength absorption in the near-UV region (< 375 nm) is mainly due to the ligand-based π–π* transitions that are associated with either (C^N) or (N^O) ligands. The less intense absorption bands at a longer wavelength (375–475 nm) could be assigned to some admixture of ligand-to-ligand charge transfer (LLCT) and singlet metal-to-ligand charge transfer (^{1}MLCT) and/or triplet metal-to-ligand charge transfer (^{3}MLCT) (5d → π*) electronic transitions.

Compared with those of **AtFOND** and **PBSOND**, the spectra of **AtFNND** and **PBSNND** show a very similar spectral feature, *i.e.*, relatively featureless and much intense absorption bands. The featureless absorption bands can be attributed to a more charge transfer (CT) characteristic. Similar and more intense absorption bands have been observed for other **ND**-based heteroleptic platinum complexes, having morpholine- or piperidine-substituted **ND**.[19,20] These have been attributed to the strong donating power of dialkylamino substituents, such as morpholinyl, piperidinyl, and dimethylamino groups. Our spectroscopic analysis is basically consistent with the calculated electron density of the HOMO (highest occupied molecular orbital) of the four platinum complexes, of which the electron density resides primarily on the **OND** or **NND** ligand, and secondarily on the Pt atom and the anisole group and phenyl group of **AtF** and **PBS**, respectively (Fig. 4). Accordingly, the stronger donor-containing **ND** ligand, *i.e.*, **NND**, causes more featureless and more intense absorption bands.

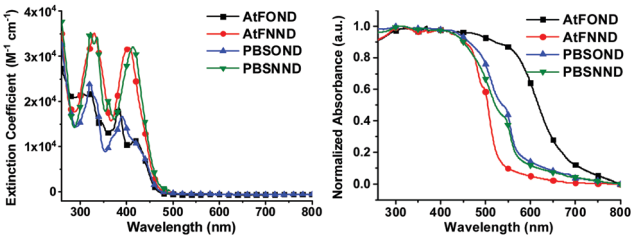

Fig. 3 UV-vis absorption spectra of the studied platinum complexes in CH_2Cl_2 at a concentration of 1×10^{-5} M (left) and as a crystal/powder (right).

Table 1 Photophysical data and thermal decomposition temperature of the studied platinum complexes

Pt complexes	λ_{max}^{ab} (ε) [nm] in CH_2Cl_2 (10^3 M^{-1} cm^{-1})	λ_{max}^{PL} (nm) in CH_2Cl_2			λ_{max}^{PL} (nm) neat film	ϕ_{PL}[a]	τ_p[b] (μs)
		2×10^{-5} M	2×10^{-4} M	2×10^{-3} M			
AtFOND	419(11)	532	548	690	770	0.09, 0.09	1.99
AtFNND	406(32)	523	528	715	750	0.18, 0.58	1.17
PBSOND	414–416(11)	543	587	711	740	0.24, 0.53	1.52
PBSNND	413(32)	546	592	715	732	0.36, 0.32	0.71

[a] PLQY determined in degassed CH_2Cl_2 at 2×10^{-5} M using $[Ru(bpy)_3](PF_6)_2$ (bpy = 2,2′-bipyridine) in acetonitrile as a reference (ϕ_{PL} = 0.062).[25] The second number is the solid state (15 wt% dopants in the 4P-NPD thin film) PLQY determined by the integrating sphere method with monochromated incident light at a wavelength of 442 nm. [b] Room temperature PL lifetime determined in degassed CH_2Cl_2.

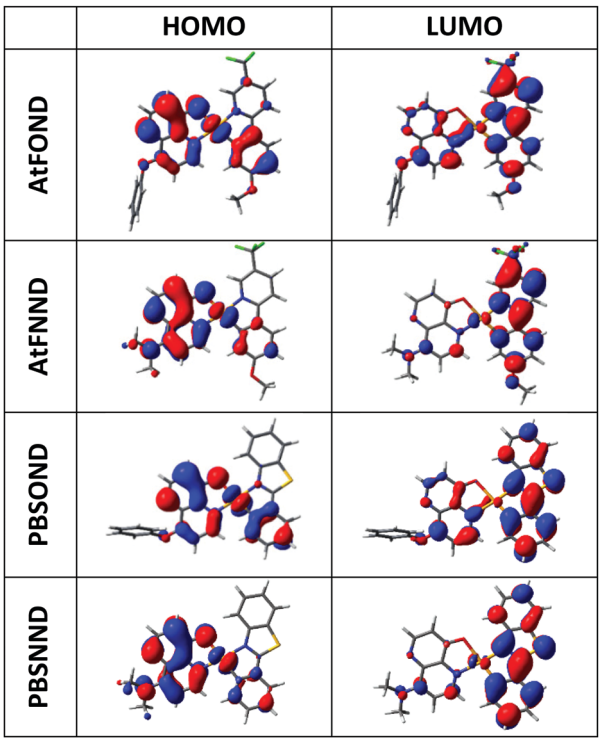

Fig. 4 Calculated electron density contour plots of the frontier molecular orbitals of the studied complexes (isovalue = 0.0250).

On the other hand, regardless of **AtF** or **PBS**, whenever **OND** is included as one of the coordination ligands, there are multiple absorption bands and their intensity is significantly reduced (Fig. 3). Moreover, the absorption energy gap of the four platinum complexes is determined by the **OND** or **NND** ligand, not by the **AtF** or **PBS** ligand. This is because the **NND**-containing platinum complexes always exhibit a shorter wavelength of λ_{max}^{ab} (Table 1 and Fig. 3) than that of the **OND**-containing platinum complexes, regardless of the **AtF** or **PBS** ligand. Such spectroscopic results are very much consistent with that of the HOMO electrons that reside mostly on the **OND** or **NND** ligand, which dictate the absorption spectra of the four platinum complexes.

Photoluminescence spectroscopic analysis

The PL spectra of the studied platinum complexes in both solutions with varied concentrations and drop-cast thin films with varied host materials are shown in Fig. 5. Different from the absorption spectra, **AtF** or **PBS** (not **OND** or **NND**) is the decisive ligand for the PL spectra of the four platinum complexes. This is consistent with our DFT/TD-DFT calculations, revealing that the electron density of the LUMO (lowest unoccupied molecular orbital) primarily distributes on the **AtF** or **PBS** ligand, and sporadically on the Pt atom and the phenoxypyridine and dimethylaminopyridine of the **OND** and **NND**, respectively (Fig. 4).

At a lower solution concentration of 2×10^{-5} M, all the platinum complexes show a PL emission with peak wavelengths of 532, 523, 543, and 546 nm for **AtFOND**, **AtFNND**, **PBSOND**, and **PBSNND**, respectively. First, λ_{max}^{PL} of **AtFOND** and **AtFNND** is shorter than that of **PBSOND** and **PBSNND**, respectively. Second, the more distinct and stronger vibronic emission bands observed for **PBSOND** and **PBSNND** than **AtFOND** and **AtFNND** indicate that **AtF** or **PBS** dictates the PL spectra. This is consistent with the calculated electron density of the LUMO which is distributed mostly on the **AtF** or **PBS** (Fig. 4). The distinct and strong vibronic emission bands observed for **PBSOND** and **PBSNND** can be explained by a more extended π-conjugation of the **PBS** ligand, and hence a more local excitation (LE) characteristic in the emission state. Upon increasing the solution concentration of these platinum complexes to 2×10^{-4} M and 2×10^{-3} M, the emission profiles were broadened due to the emerging emission bands with λ_{max}^{PL} around the deep red or NIR region (Fig. 5). The PL spectra become a mixture of the monomeric emissions (λ_{max}^{PL} of 523–546 nm) and the aggregate/excimer emissions (λ_{max}^{PL} of 675–716 nm). When the solution concentration is increased, the aggregate/excimer emissions are intensified, and the monomeric emissions are weakened. Moreover, while aggregate/excimer emissions are clearly seen at 2×10^{-4} M for **AtFOND** and **AtFNND**, it takes a higher concentration of 2×10^{-3} M to develop aggregate/excimer emissions of **PBSOND** and **PBSNND**, of which substantial monomeric emissions still remain in the spectra. Such solution PL spectra demonstrate that either **AtFOND** or **AtFNND** is more prone to aggregate/excimer formation than **PBSOND** and **PBSNND**. In addition to a less tendency to aggregate/excimer formation, emissions associated with a higher LE characteristic may be the reason for higher solution PLQYs of 24% and 36% for **PBSOND** and **PBSNND** than 9% and 18% for **AtFOND** and **AtFNND**, respectively. Moreover, we have observed that **OND**-containing platinum complexes always have a lower solution PLQY than that of **NND**-containing ones, such as 9% and 18% of **AtFOND** and **AtFNND** and 24% and 36% of **PBSOND** and **PBSNND**, respectively. Such solution PLQY

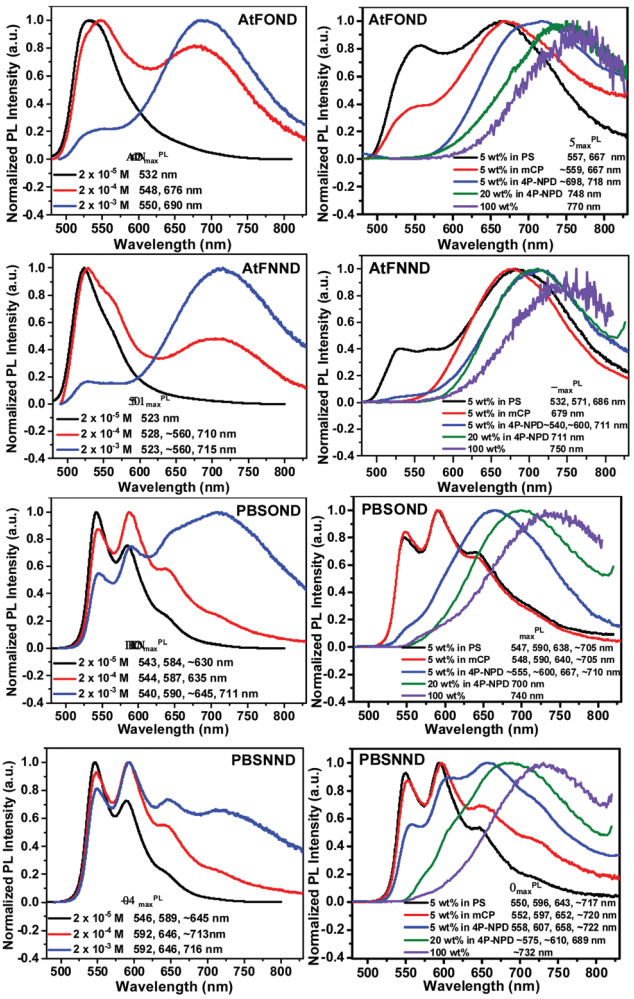

Fig. 5 Normalized PL spectra of the studied platinum complexes in CH_2Cl_2 with varied concentrations (left) and as a solution drop-cast thin film of 5 wt% doped PS, *m*CP, 4P-NPD, 20 wt% doped 4P-NPD, and the neat film (100 wt%), respectively, where PS is polystyrene, *m*CP is *N*,*N*′-dicarbazolyl-3,5-benzene, and 4P-NPD is *N*,*N*′-di-1-napthalenyl-*N*,*N*′-diphenyl-[1,1′:4′,1″:4″,1‴-quaterthiophene]-4,4‴-diamine.[21]

results can be understood by the fact that **OND** has a higher vibrational freedom than **NND** because of the phenoxy substituent. Otherwise, the solution PL lifetimes of the four platinum complexes have been measured. They are all in the microsecond regimes; 7.78 μs for **AtFOND**, 1.17 μs for **AtFNND**, 1.52 μs for **PBSOND**, and 0.71 μs for **PBSNND** (Fig. S15, ESI†). Such PL lifetimes are in general consistent with the solution PLQYs, *i.e.*, the lowest PLQY **AtFOND** having the longest PL lifetime; the highest PLQY **PBSNND** having the shortest PL lifetime.

While the formation of aggregates/excimers is concentration-dependent in solution, the host material is decisive for showing deep red or NIR emissions for the four platinum complexes in the solid state, including the doped thin films. The 4P-NPD hosted thin films always promote the aggregate/excimer emissions of the four platinum complexes more than PS or mCP hosted thin films. Nevertheless, as a 100 wt% sample (neat film), all of the four platinum complexes display broad NIR emissions with a λ_{max}^{PL} of 770, 750, 740, and 732 nm for **AtFOND**, **AtFNND**, **PBSOND**, and **PBSNND**, respectively. All of these NIR emission spectra virtually show no trace of greenish yellow emissions, even though some of these NIR emissions are relatively weak. Similarly, as those in solution, either **AtFOND** or **AtFNND** always exhibits more genuine deep red or NIR emissions (with much less intense greenish yellow monomeric emissions) than **PBSOND** and **PBSNND** in the doped thin films (Fig. 5). For **AtFOND**, the long wavelength emissions from the MMLCT due to the short (and hence strong) Pt–Pt contacts may be the main reason. For **AtFNND**, there are many short molecular contacts (2.44–3.19 Å) found on the methoxy group (OCH_3) of **AtF** (Fig. S16, ESI†). The short contacts involve the oxygen of the OCH_3 group, the CH_3 of the dimethylamino group, the CH_3 of the OCH_3 group, the H of the benzene ring (of anisole), the H of the naphthyridine ring, the CH_3 of the OCH_3 group, the oxygen of ArO–Pt, and the CF_3 of the trifluoromethyl group. There is also a π–F contact found in the crystal of **AtFNND**. These molecular contacts bring the molecules of **AtFNND** closer in the solid state and in high-concentration (2×10^{-3} M) solution, reducing the green emissions of non-aggregated **AtFNND**. Even though **AtFNND** has many short molecular contacts that extend the emission wavelength, the solid-state PLQY of **AtFNND** does not seem to be affected. Probably, many of these short contacts occur in the peripheral structures of **AtFNND**, not much involving the light-emitting π-conjugated moieties. The solid-state PLQY of **AtFNND** was determined to be 58%, the highest among the four platinum complexes (Table 1). In sharp contrast, the solid-state PLQY of **AtFOND** was measured to be less than 10%, the lowest among the four platinum complexes. We may attribute such a low PLQY mainly to the energy gap law, in which the non-radiative pathway dictates the relaxation of the excited state of the deep red or NIR emitters. Otherwise, there is no particularly effective short molecular contact, except for the short and near-vertical Pt–Pt contact (Fig. 1 and Fig. S16, ESI†), which is unique among the four platinum complexes. We surmise that the low PLQY may be due to the MMLCT of **AtFOND**.

Electrochemical properties and the energy level of HOMO/LUMO

The redox properties of the studied platinum complexes are illustrated by the cyclic voltammograms (CVs) in Fig. 6 and the numerical data are summarized in Table 2.

The first oxidation potential, $E_{1/2}^{OXD}$, exhibits the trend of similarity with the type of ancillary ligands **NND** and **OND**, 0.45–0.52 V and 0.61–0.60 V *vs.* Fc^+/Fc, respectively. Such CV results are much consistent with the calculated HOMO electron density (Fig. 4), which distributes primarily on the **OND** or **NND** involving coordinated platinum. The anodic signals of **AtFOND** and **PBSOND** are at higher potentials than those of **AtFNND** and **PBSNND**, which is consistent with the stronger electron-donating strength of the dimethylamino group than that of the phenoxy group. Taking the absorption onset wavelength as the optical energy gap (E_g), the LUMO energy level (E_{LUMO}) of each platinum complex can be calculated based on the CV-determined HOMO energy level (E_{HOMO}) (Table 2). The materials used for device fabrication, including 4P-NPD, *m*CP, and TPBi, were determined by the same method for E_{HOMO} and E_{LUMO}. They are all aligned and

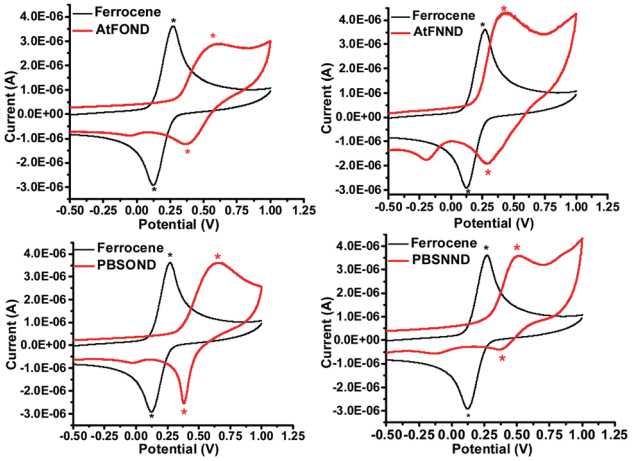

Fig. 6 Cyclic voltammograms of **AtFOND**, **AtFNND**, **PBSOND**, **BSNND**, and ferrocene (reference) in CH_2Cl_2 (1 mM) in the presence of 0.1 M $TBAPF_6$ at 295 K.

Table 2 Electrochemical data, HOMO/LUMO energy levels, and energy gaps of the studied platinum complexes

Pt complexes	$E_{1/2}^{oxd}$ [a] (V)	E_{HOMO} (eV)	λ_{onset} [b] (nm)	E_g [c] (eV)	E_{LUMO} [d] (eV)
AtFOND	0.49	−5.09	462	2.68	−2.41
AtFNND	0.37	−4.98	460	2.69	−2.29
PBSOND	0.52	−5.12	466	2.65	−2.47
PBSNND	0.45	−5.06	461	2.69	−2.37

[a] $E_{1/2}^{oxd}$ (V) refers to $[(E_{pa} + E_{pc})/2]$, where E_{pa} and E_{pc} are the anodic and cathodic peak potentials, respectively; 0.196 V for Fc^+/Fc. [b] Determined from the onset wavelength of the absorption spectrum. [c] Estimated from the onset absorption spectrum by the equation $E_g = 1240/\lambda_{onset}$. [d] Deduced from the E_{HOMO} and E_g.

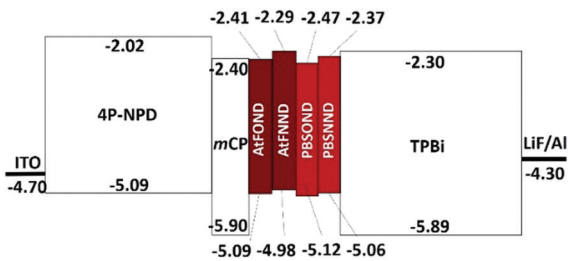

Fig. 7 Energy level (eV) alignment of materials involved in the NIR OLEDs.

displayed in Fig. 7. Accordingly, singlet excitons can be well confined on the light-emitting layer of the platinum complex in the device of ITO/4P-NPD/*m*CP/Pt complex/TPBi/LiF/Al.

Electroluminescence properties

The ultrathin light-emitting layers (EMLs) have been demonstrated to enhance the efficiency of non-dopant platinum complex OLEDs.[26–28] Accordingly, the ultrathin light-emitting layers of the NIR OLEDs were fabricated by vacuum thermal evaporation as ITO/4P-NPD (40 nm)/*m*CP (5 nm)/Pt complex (2 nm)/TPBi (45 nm)/LiF (0.8 nm)/Al (100 nm) for **AtFOND**, **AtFNND**, **PBSOND**, and **PBSNND**, respectively. Data of EL characteristics are summarized in Table 3 and the corresponding device performance is displayed in Fig. 8–10.

Table 3 Key EL performance data of the NIR OLEDs

NIR emitter	λ_{max}^{EL} (nm)	$V_{turn\ on}$ [a] (V)	EQE [b] (%) (mA cm^{-2})	Brightness [cd] (cd m^{-2})
AtFOND	774	8.0	1.77(6.34)	220
AtFNND	744	4.0	6.54(0.14)	440
PBSOND	726	5.5	3.95(1.43)	830
PBSNND	704	4.0	10.12(2.85)	1400

[a] Turn-on voltage is the one at which the luminescence is over 1 cd m^{-2}. [b] The maximum value of external quantum efficiency (EQE) and the corresponding current density (in parenthesis). [c] Electroluminescence obtained at maximum values. [d] Based on human visual perception, cd m^{-2} is not suitable for genuine NIR OLEDs.

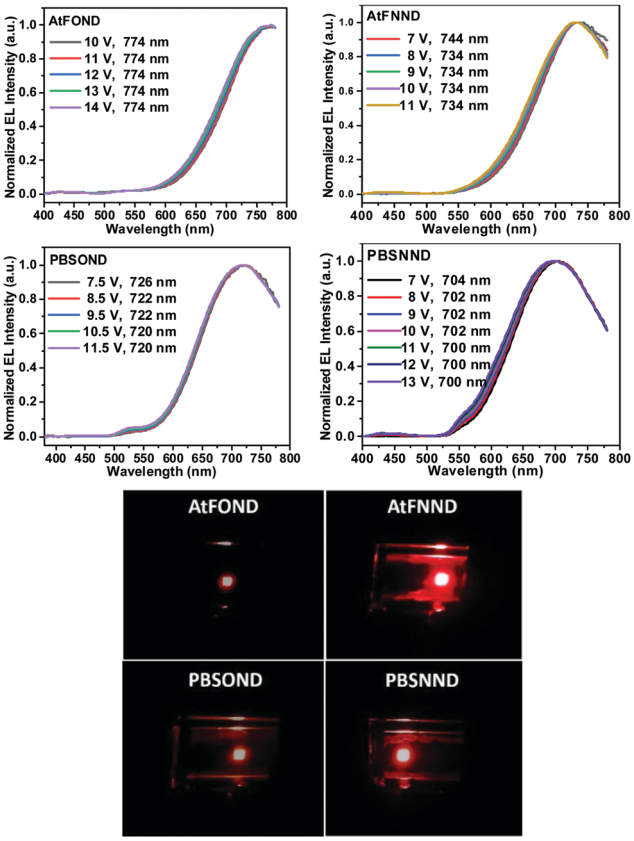

Fig. 8 Top figures: intensity normalized EL spectra **AtFOND**, **AtFNND**, **PBSOND**, and **PBSNND** NIR OLEDs at varied voltage. Bottom figures: corresponding photographs of each device at ~4–6 V.

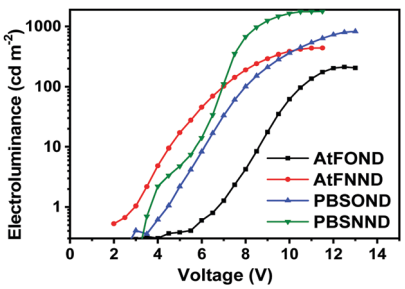

Fig. 9 Voltage dependency of electroluminescence (cd m^{-2}) of NIR OLEDs.

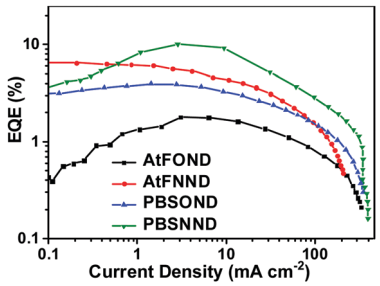

Fig. 10 External quantum efficiency as a function of current density.

As shown in the EL spectra in Fig. 8, the λ_{max}^{EL} values are 774, 736, 726, and 704 nm for **AtFOND**, **AtFNND**, **PBSOND**, and **PBSNND** OLEDs, respectively. Since all the λ_{max}^{EL} values are >700 nm, these are all NIR OLEDs. All the NIR EL have broad and featureless emission bands, typical for the aggregates/excimers of the platinum complexes. By carefully examining the EL spectra in Fig. 8, there are some minor greenish yellow emissions observed around 500–550 nm and 525–575 nm, which are discernible in **PBSOND** and **PBSNND** spectra, respectively. Such greenish yellow emissions are virtually invisible in **AtFOND** and **AtFNND** spectra. This is very much similar to the PL spectra of the four platinum complexes in the solid state (Fig. 5). It has been demonstrated from both PL and EL spectra that the aggregates/excimers are more in **AtFOND** and **AtFNND** than in **PBSOND** and **PBSNND**.

Although a camera is different from a spectroradiometer in terms of brightness and detection sensitivity to NIR, these photographs (Fig. 8 bottom) qualitatively show the relative brightness of each device with a driving voltage of around 4–6 V. While the **AtFOND** NIR OLED has the least brightness in all driving voltages, the brightest NIR OLED is based on **AtFNND** instead of **PBSNND**. Interestingly, such photographs are generally in accordance with the electroluminescence data of the four NIR OLEDs driven at ~4–6 V (Fig. 9), although the electroluminescence (cd m^{-2}) does not really work for the nearly invisible light from these NIR OLEDs.

Nevertheless, from the photographs shown in Fig. 8, the **PBSOND** device shows a more orange colour than the other three devices, due to its relatively short NIR EL wavelength (726 nm) and the greenish yellow emission around 520–550 nm, which is most pronounced among the four platinum complexes. Since a conventional camera simply cannot detect NIR, the **AtFOND** device is the darkest and the most reddish one among the four devices, because of the longest NIR EL wavelength (774 nm) and the longest PL wavelength (750 nm) among the four platinum complexes. The very low PLQY (<10%), either in solution or thin film, is another reason for its feeble PL and EL.

The EQE characteristics of the four NIR OLEDs are plotted as a function of current density in Fig. 10. The figure shows that 1.77%, 6.54%, 3.95%, and 10.12% are the determined maximum EQE values for **PBSOND**, **PBSNND**, **AtFOND**, and **AtFNND** NIR OLEDs, respectively.

Except for the **AtFNND** one, the NIR OLEDs exhibit EQE peaked around 1–7 mA cm^{-2}, corresponding to 5–9 V of the OLEDs (Fig. S17, ESI†). Except for the **AtFNND** one, within a range of 10–100 mA cm^{-2}, the NIR OLEDs exhibit approximately similar EQE roll-off. In addition to a rather similar rising slope of the current density *vs.* driving voltage (Fig. S17, ESI†), we may infer that the efficiency of electron–hole recombination (charge-balance factor) is about the same for **AtFOND**, **PBSOND**, and **PBSNND** OLEDs, but they are all better than that of **AtFNND** OLEDs. Since the thickness of the different layers in the four NIR OLEDs is the same, we surmise that such results may be due to the LUMO energy level of **AtFNND**, which is the highest lying one among the four platinum complexes and is somewhat higher than that of TPBi, the electron transporting material in these NIR OLEDs. Analysing the correlation between the device's EQE and the material's solid state PLQY, the lowest EQE (1.77%) of **AtFOND** OLEDs can be mainly ascribed to the very low thin film PLQY (<10%) and the very long EL wavelength of 774 nm, of which nearly half of the EL is beyond the detection limit of the spectroradiometer (780 nm of PR-670). A relatively high EQE (6.54%) of **AtFNND** OLEDs is probably due to its much higher thin film PLQY (58%) and a comparatively shorter EL wavelength of 744 nm. With a reasonable inference, a relatively lower thin film PLQY (52%) of **PBSOND** can be the reason for its lower EQE (3.95%) of OLEDs. The most surprising EQE is the 10.17% of **PBSNND** OLEDs. Such an EQE is unusually high, considering the thin film PLQY (ϕ_{PL}) of **PBSNND**, which is only 32% (Table 1). Assuming 100% for both the radiative exciton fraction (η_r) and the efficiency of the electron–hole recombination (γ), lower limits for the light outcoupling efficiency (η_{out}) can be estimated around 32%, based on an EQE = $\gamma \times \eta_r \times \phi_{PL} \times \eta_{out}$. For a conventional OLED with randomly oriented light-emitting molecules and no additional light outcoupling enhancements, the average or regular η_{out} is ~20%. Therefore, for such **PBSNND** NIR OLEDs, an η_{out} higher than 20% strongly suggests that some **PBSNND** molecules have special molecular orientation that enhances the η_{out} of OLEDs.

2D-GIWAXS and molecular orientation

A relatively weak and diffused signal has been identified on the 2D-GIWAXS patterns at the Q_z of 0.55 $Å^{-1}$ (Fig. 11 top). The corresponding *d*-spacing is calculated to be 11.4 Å (Fig. S18, ESI†). From the X-ray single-crystal data of **PBSNND**, we have found two correlated distances of 12.0 and 12.2 Å (see Fig. 11 centre). In a unit cell of the **PBSNND** crystal, molecules of **PBSNND** are stacked pairwise, two pairs in the upper part and another two pairs in the lower part along the *c*-axis of the unit cell (see Fig. 11 centre and bottom).

The projection (~60–70°) of the molecular transition dipole of the MLCT onto the molecular mean plane (see Fig. 11 bottom) is coincident with the direction of *s*-polarized waves of the emitting light of the OLEDs, if the molecular mean plane is parallel to the horizontal direction. As such, the light outcoupling of **PBSNND** OLEDs is enhanced. Therefore, the GIWAXS results together with the single-crystal X-ray structure of **PBSNND** reasonably explain that the high EQE is due to an enhanced η_{out} of ~32%.

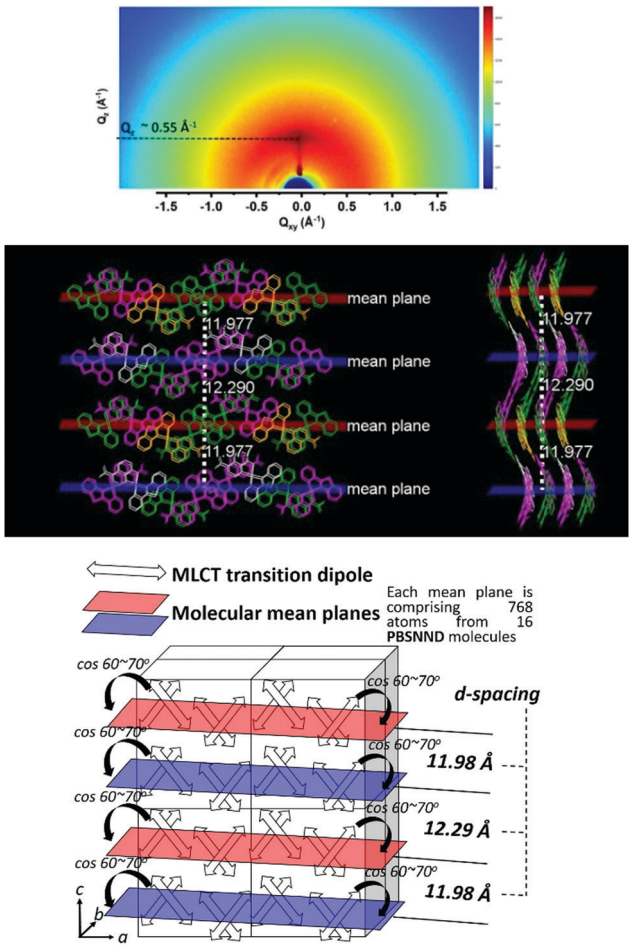

Fig. 11 Top: 2D-GIWAXS patterns for a vacuum-deposited thin film of **PBSNND**. Centre: Molecular array in the crystal structure of **PBSNND** with a ~90° difference of two viewing angles. Bottom: The schematic display of the centre picture with the labels of MLCT transition dipole, molecular mean plane, and *d*-spacing.

Conclusions

In summary, we have successfully synthesized and characterized **AtFOND**, **AtFNND**, **PBSOND**, and **PBSNND** platinum complexes for PL and EL studies. All four platinum complexes exhibit green to yellow PL in diluted solution but deep red or NIR PL in the solid state. Based on the colours and absorption spectra of the platinum complexes in the solid state, we believe that the MMLCT occurs only for **AtFOND** among the four platinum complexes. The proposed MMLCT is consistent with the Pt–Pt contacts, which are short (3.39 and 3.88 Å) and almost normal to the molecular planes of the platinum complex evident from the single-crystal X-ray structure. This is probably the reason for **AtFOND** showing the longest wavelengths of 770 and 774 nm for NIR PL and EL, respectively, in the solid state. However, such MMLCT does not help in the solid-state PLQY or the EQE of the NIR OLEDs. Both PLQY and EQE are the lowest, 9% and 1.8%, among the four platinum complexes. On the other hand, **PBSNND** shows a relatively high EQE (~10.1%) of the NIR (λ_{max}^{EL} 704 nm) OLEDs, considering its moderate solid-state PLQY of ~32%. From both 2D-GIWAXS and single-crystal X-ray studies, we have verified that such a high EQE can be attributed to an appropriate molecular alignment of **PBSNND** that enhances the light outcoupling efficiency to 32%, which is ~1.6 times higher than ~20% of most conventional OLEDs.

Experimental section

General information

^{1}H and ^{13}C NMR spectra were recorded using Bruker AV-400 MHz and AV-500 MHz NMR Fourier transform spectrometers at room temperature. Elemental analyses were performed at the Instrumentation Center, National Taiwan University. Electron ionization (EI) or fast atom bombardment (FAB) mass spectroscopy (MS) was performed at the Mass Spectroscopic Laboratory, an in-house service of the Institute of Chemistry, Academic Sinica. Solution UV-vis absorption spectra were recorded using a Hewlett-Packard 8453 diode array spectrophotometer. Powder or crystal solid-state absorption spectra were obtained *via* surface reflection spectroscopy (JASCO V-670 spectrophotometer). Room temperature photoluminescence (PL) spectra of solution, thin film, or powder were recorded using a Hitachi fluorescence spectrophotometer F-7000 or Edinburgh FL920.

Solution PLQY was determined using a degassed acetonitrile solution of $[Ru(bpy)_3](PF_6)_2$ (bpy = 2,2′-bipyridine) as the standard solution (Φ_{PL} = 6.2%).[33] The thin film PLQY was determined by the integrating-sphere (Titan Electro-Optics Co., Ltd, Taiwan) method using a monochromated light source (IK5451R-E Kimmon Koha Co., Ltd, Japan) with an excitation wavelength of 442 nm and a Hitachi-F-7000 spectrophotometer as a photodetector. The photoluminescence lifetime was determined on degassed solution samples with an Edinburgh FL920 time-correlated pulsed single-photon-counting instrument.

Redox potentials of the platinum complexes were determined by cyclic voltammetry (CV) using a BAS 100B electrochemical analyser with a scanning rate at 100 mV s^{-1}. **FBNNND** was dissolved in deoxygenated dry CH_2Cl_2 with 0.1 M tetrabutylammonium perchlorate as the electrolyte. We used a platinum working electrode and a saturated nonaqueous $Ag/AgNO_3$ reference electrode. Ferrocene was used for potential calibration (the reported potentials are referenced against Ag/Ag^{+}) and for reversibility criteria. The energy level of ferrocene (4.8 V below the vacuum level)[29] was used as the reference.

In preparing samples for GIWAXS measurements, samples of **PBSNND** were deposited on the (100) surface of a silicon wafer. GIWAXS measurements were conducted using the facilities (beamline 17A) of the National Synchrotron Radiation Research Centre (NSRRC) at Hsinchu, Taiwan. The experiments were carried out with an X-ray photon energy of 12.043 keV and a wavelength (λ) of 1.3213 Å. The sample-to-detector distance is 80.00 mm.

X-Ray crystallography studies

Single crystals for the XRD analysis were obtained by slow evaporation of a methanol-dichloromethane solution of the

complex at room temperature. Data collection was carried out using a Bruker X8APEX CCD diffractometer at 100 K for the **FBNNND** single crystal. Mo radiation (λ = 0.71073 Å) was used for both crystals. The unit cell parameters were obtained by a least-squares fit to the automatically centered settings for reflections. Intensity data were collected using the $\omega/2\theta$ scan mode. Corrections were made for Lorentz and polarization effects. The structures were solved by direct methods SHELX-97.[30] All non-hydrogen atoms were located from the difference Fourier maps and were refined by full-matrix least-squares procedures. The position of hydrogen atoms was calculated and located. Calculations and full-matrix least-squares refinements were performed utilizing the WINGX program package[31] in the evaluation of the values of $R(F_o)$ for reflections with $I > 2\sigma(I)$ and $R_w(F_o)$, where $R = \sum\|F_o| - |F_c\|/\sum|F_o|$ and $R_w = [\sum\{w(F_o^2 - F_c^2)^2\}/\sum\{w(F_o^2)^2\}]^{1/2}$. Intensities were corrected for absorption.

OLED device fabrication and measurements

OLED devices were fabricated by vacuum–thermal deposition using Sumimoto Cryogenics at a chamber pressure of 10^{-6} torr. The ITO substrate with a sheet resistance of around 30 Ω sq^{-1} was purchased from Ruilong Optoelectronics, Taiwan. ITO-coated glass substrates were cleaned with detergent, deionized water, acetone, and isopropanol, followed by oxygen plasma treatment. The current density–voltage characteristics of the devices were measured using a Keithley 2400 source meter, and the device brightness (or electroluminescence, cd m^{-2}) and EL spectra were monitored and recorded with a spectroradiometer (PR-670, Photo Research), respectively.

Synthesis and materials

For the materials used in device fabrication, *m*CP was obtained from Shine Materials Technology Co. CBP,[32] TPBI,[33]and 4P-NPD[21] were prepared *via* the published methods. Except for **(AtF)$_2$PtCl** and **(PBS)$_2$PtCl**, these synthesized materials were purified by vacuum train sublimation before use in the device fabrication process. The general synthesis methodology of the corresponding monometallic platinum complex precursors, **(AtF)$_2$PtCl** and **(PBS)$_2$PtCl**, is reported herein. Including the much improved synthesis of **OPhONDH**, the synthesis and characterization of **AtFOND**, **AtFNND**, **PBSOND**, and **PBSNND** are shown below.

OPhONDH. Triethyl orthoformate (24 mL, 143.65 mmol) was added to a mixture of 4-phenoxypyridine-3-amine (4.45 g, 23.94 mmol) and Meldrum's acid 2,2-dimethyl-[1,3]dioxane-4,6-dione (4.14 g, 28.73 mmol). The mixture was then heated at reflux under nitrogen for 4 h. After cooling to room temperature, the reaction mixture was removed by vacuum distillation. The resulting solid was purified by flash column chromatography (silica gel, ethyl acetate/dichloromethane: 1/1) to afford the intermediate **pre-OPhND** as a white solid after recrystallization from methanol (7 g, 87%). A diphenyl ether solution (35 mL) containing **pre-OPhND** (3 g, 8.9 mmol) was heated at 250 °C and stirred under a nitrogen atmosphere for 10 min. During the reaction, the color of the solution changed from orange yellow to brown. After cooling to room temperature, the reaction solution was filtered to isolate the solid product. The solid was rinsed with diphenyl ether and the resulting solid was purified by flash column chromatography (silica gel, dichloromethane/methanol: 97/3). The product was obtained as a white solid (1.3 g, 5.46 mmol, 61%). ^{1}H NMR (400 MHz, CD_3OD): δ 8.51 (d, 1H, J = 5.12 Hz), 8.02 (d, 1H, J = 7.28 Hz), 7.58 (t, 2H, J = 6.28 Hz), 7.41 (t, 1H, J = 7.34 Hz), 7.32 (d, 2H, J = 8.24 Hz), 6.89 (d, 1H, J = 5.28 Hz), 6.57 (d, 1H, J = 7.24 Hz). ^{13}C NMR (100 MHz, CD_3OD): δ 179.28, 157.41, 154.82, 148.83, 142.63, 141.08, 131.80, 130.68, 127.73, 122.15, 113.15, 110.59. EI-MS: calcd 238.07, m/z = 238.07 (M^+).

(AtF)$_2$PtCl and (PBS)$_2$PtCl. On the basis of a modified literature methodology, a solution of potassium tetrachloroplatinate(II) (1.0 equiv.) in water (2 mL) was added to a stirring solution of ligand (2.5 equiv.) in 2-ethoxyethanol (6 mL) under a nitrogen environment and heated to 80 °C for 48 h in an aluminum foil-wrapped flask. Water (10 mL) was added to the cooled solution, and the resultant precipitate was collected on a sintering funnel, washed with water (2 × 10 mL), and dried. The isolated products of **(AtF)$_2$PtCl** or **(PBS)$_2$PtCl** have a higher reaction yield and were used in the following synthesis without purification, although both of them can be purified further by column chromatography.[34,35] The mass spectral data of both the intermediate monometallic complexes showed that the parent peaks were consistent with the expected molecular formula.

AtFOND. A mixture of **(AtF)$_2$PtCl** (0.22 g, 0.29 mmol), Na_2CO_3 (0.31 g, 2.93 mmol), and **OPhND** (0.15 g, 0.62 mmol) in 1,2-dimethoxyethane (10 mL) was stirred and heated at 80 °C under a nitrogen atmosphere for 16 h. The product was purified by column chromatography (silica gel, dichloromethane/methanol: 98/2) and the last red band was collected. The product was isolated as a red solid (0.19 g, 95%). The single crystals for the X-ray diffraction structure analysis were obtained by slow evaporation of methanol–dichloromethane solution of **AtFOND** at room temperature. ^{1}H NMR (400 MHz, $CDCl_3$, δ): 9.49 (s, 1H), 8.79 (d, 1H, J = 6.2 Hz), 8.56 (d, 1H, J = 5.4 Hz), 7.95 (d, 1H, J = 8.4 Hz), 7.54 (dd, 3H, J = 8.4, 7.8 Hz), 7.45 (d, 1H, J = 8.6 Hz), 7.36 (t, 1H, J = 7.6 Hz), 7.30 (s, 2H), 6.95 (d, 2H, J = 5.5 Hz), 6.86 (d, 1H, J = 1.7 Hz), 6.69 (t, 2H, J = 5.7 Hz), 3.85 (s, 3H). ^{13}C NMR (125 MHz, $CDCl_3$, δ): 173.45, 169.37, 163.61, 161.02, 153.71, 153.41, 148.01, 147.12, 146.39, 141.59, 138.72, 137.18, 135.14, 126.71, 126.63, 123.92, 123.25, 122.98, 121.80, 117.85, 117.05, 113.43, 108.05, 106.63, 55.29. FAB-HRMS: calcld 684.0948, m/z = 685.1035 ($M + H^+$). Anal. found (calcd) for $C_{27}H_{18}F_3N_3O_3Pt$, C 46.52(47.37), H 2.62(2.65), N 5.99(6.14).

AtFNND. A mixture of **(AtF)$_2$PtCl)** (0.39 g, 0.51 mmol), Na_2CO_3 (0.54 g, 5.14 mmol), and **dmaND** (0.20 g, 1.08 mmol) in 1,2-dimethoxyethane (10 mL) was stirred and heated at 80 °C under a nitrogen atmosphere for 16 h. The product was purified by column chromatography (silica gel, dichloromethane/methanol 98 : 2) and the last yellow band was collected and dried to yield a yellow solid. The product was isolated as a golden yellow solid (0.31 g, 0.48 mmol, 92%). The single crystals for the X-ray diffraction structure analysis were obtained by slow evaporation of methanol–dichloromethane solution of **AtFNND** at room temperature. ^{1}H NMR (400 MHz, $CDCl_3$, δ): 9.55 (S, 1H),

8.61(d, 1H, J = 6.4 Hz), 8.28 (d, 1H, J = 5.2 Hz), 7.94 (d, 1H, J = 8.2 Hz), 7.58 (d, 1H, J = 8.4 Hz), 7.50 (d, 1H, J = 8.5 Hz), 7.05 (S, 1H), 6.87 (d, 1H, J = 5.3 Hz), 6.70 (d, 1H, J = 8.4 Hz), 6.54 (d, 1H, J = 6.4 Hz), 3.93 (S, 3H), 3.57 (S, 6H)). ^{13}C NMR (125 MHz, $CDCl_3$, δ): 173.27, 169.79, 161.42, 154.95, 149.01, 147.21, 146.53, 146.50, 146.15, 143.02, 139.14, 137.54, 135.02, 126.95, 124.11, 123.44, 123.17, 122.90, 121.95, 118.37, 117.35, 112.39, 108.30, 105.00.

FAB-HRMS: calcld 635.1108, m/z = 636.1194 (M + H$^+$). Anal. found (calcd) for $C_{23}H_{19}F_3N_4O_2Pt$ C 43.44(43.47), H 3.11(3.01), N 8.82(8.82).

PBSOND. A mixture of **(PBS)$_2$PtCl)** (0.14 g, 0.22 mmol), Na_2CO_3 (0.22 g, 2.1 mmol), and **OPhND** (0.11 g, 0.47 mmol) in 1,2-dimethoxyethane (10 mL) was stirred and heated to 80 °C under a nitrogen atmosphere for 16 h. The product was purified by column chromatography (silica gel, dichloromethane/methanol: 99 : 1) and the last yellow band was collected. The product was isolated as a red solid (0.09 g, 0.13 mmol, 62%). ^{1}H NMR (400 MHz, $CDCl_3$, δ): 9.46 (d, 1H, J = 8.4 Hz), 8.90 (d, 1H, J = 5.9 Hz), 8.58 (d, 1H, J = 5.5 Hz), 7.81 (d, 1H, J = 7.9 Hz), 7.65 (t, 1H, J = 7.9 Hz), 7.44–7.53 (m, 5H), 7.37 (d, 1H, J = 7.0 Hz), 7.31 (d, 2H, J = 7.6 Hz), 7.13 (t, 2H, J = 6.8 Hz), 7.01 (d, 1H, J = 5.4 Hz), 6.71 (d, 1H, J = 6 Hz). ^{13}C NMR (125 MHz, $CDCl_3$, δ): 107.06, 113.46, 122.06, 123.59, 126.18, 128.07, 130.96, 137.80, 138.59, 142.09, 147.14, 150.72, 153.73, 163.77, 175.08, 181.35. FAB-HRMS: calcld: 642.0689, m/z = 643.0772 (M + H$^+$). Anal. found (calcd) for $C_{27}H_{17}N_3O_2PtS$ C 47.19(50.47), H 2.56(2.67), N 6.24(6.54).

PBSNND. A mixture of **(PBS)$_2$PtCl** (0.30 g, 0.46 mmol), Na_2CO_3 (0.49 g, 4.6 mmol), and **dmaND** ligand (0.18 g, 0.97 mmol) in 1,2-dimethoxyethane (10 mL) was stirred and heated at 80 °C under a nitrogen atmosphere for 16 h. The product was purified by column chromatography (silica gel, dichloromethane/methanol: 99/1) and the last yellow band was collected. The product was isolated as a yellow solid (0.12 g, 0.20 mmol 43%). The single crystals for the X-ray diffraction structure analysis were obtained by the slow evaporation of methanol–dichloromethane solution of **PBSNND** at room temperature. ^{1}H NMR (400 MHz, $CDCl_3$, δ): 3.56 (1H, s), 6.58 (1H, d, J = 6.59 Hz), 6.96 (1H, d, J = 5.32 Hz), 7.14 (1H, m, J = 3.09 Hz), 7.45 (1H, m, J = 4.03 Hz), 7.55 (1H, q, J = 2.84 Hz), 7.65 (1H, m, J = 5.20 Hz), 7.81 (1H, d, J = 7.90 Hz), 8.32 (1H, d, J = 5.29 Hz), 8.73 (1H, d, J = 6.57 Hz), 9.52 (1H, d, J = 8.32 Hz). ^{13}C NMR (125 MHz, $CDCl_3$, δ): 43.45, 105.12, 112.37, 122.14, 123.46, 125.77, 128.14, 130.70, 132.24, 139.03, 142.30, 145.30, 146.87, 149.08, 151.09, 155.01, 174.67, 181.15. FAB-HRMS: calcld 593.0849, m/z = 594.0928 (M + H$^+$). Anal. found (calcd) for $C_{23}H_{18}N_4OPtS$ C 45.98(46.54), H 3.11(3.06), N 9.59(9.44).

Conflicts of interest

There are no conflicts to declare.

Acknowledgements

The authors thank the Ministry of Science and Technology (MOST 106-2113-M-001-016-MY3) of Taiwan for financial support. The International Graduate Program (TIGP) of Academia Sinica, Institute of Chemistry of Academia Sinica, and National Yang Ming Chiao Tung University are acknowledged.

References

1 T. Weil, T. Vosch, J. Hofkens, K. Peneva and K. Müllen, *Angew. Chem., Int. Ed.*, 2010, **49**, 9068–9093.
2 Z. Guo, S. Park, J. Yoon and I. Shin, *Chem. Soc. Rev.*, 2014, **43**, 16–29.
3 E. C. Lee, H. Jung and D. Kim, *Sensors*, 2011, **11**, 2319–2333.
4 L. Maggini, I. Cabrera, A. Ruiz-Carretero, E. A. Prasetyanto, E. Robinet and L. De Cola, *Nanoscale*, 2016, **8**, 7240–7247.
5 B. N. G. Giepmans, S. R. Adams, M. H. Ellisman and R. Y. Tsien, *Science*, 2006, **312**, 217–224.
6 J. L. Liu, J. Q. Zhang, Z. L. Tang, Y. Zhuo, Y. Q. Chai and R. Yuan, *Chem. Sci.*, 2019, **10**, 4497–4501.
7 A. Zampetti, A. Minotto and F. Cacialli, *Adv. Funct. Mater.*, 2019, **29**, 1807623.
8 X. Du, J. Qi, Z. Zhang, D. Ma and Z. Y. Wang, *Chem. Mater.*, 2012, **24**, 2178–2185.
9 Y. Yuan, J. Liao, S. Ni, A. K.-Y. Jen, C. Lee and Y. Chi, *Adv. Funct. Mater.*, 2019, 1906738.
10 J. V. Caspar, E. M. Kober, B. P. Sullivan and T. J. Meyer, *J. Am. Chem. Soc.*, 1982, **104**, 630–632.
11 F. C. Spano and C. Silva, *Annu. Rev. Phys. Chem.*, 2014, **65**, 477–500.
12 M. Ibrahim-Ouali and F. Dumur, *Molecules*, 2019, **24**, 1412.
13 X. Yang, H. Guo, X. Xu, Y. Sun, G. Zhou, W. Ma and Z. Wu, *Adv. Sci.*, 2019, **6**, 1801930.
14 K. R. Graham, Y. Yang, J. R. Sommer, A. H. Shelton, K. S. Schanze, J. Xue and J. R. Reynolds, *Chem. Mater.*, 2011, **23**, 5305–5312.
15 M. A. Baldo and S. R. Forrest, *Phys. Rev. B: Condens. Matter Mater. Phys.*, 2000, **62**, 958–966.
16 Q. Wang, I. W. H. Oswald, X. Yang, G. Zhou, H. Jia, Q. Qiao, Y. Chen, J. Hoshikawa-halbert and B. E. Gnade, *Adv. Mater.*, 2014, **26**, 8107–8113.
17 P. Ganesan, W. Hung, J. Tso, C. Ko, T. Wang, P. Chen, H. Hsu, S. Liu, G. Lee, P. Chou, A. K. Jen and Y. Chi, *Adv. Funct. Mater.*, 2019, **29**, 1900923.
18 K. Tuong, Ly, R. W. Chen-Cheng, H. W. Lin, Y. J. Shiau, S. H. Liu, P. T. Chou, C. S. Tsao, Y. C. Huang and Y. Chi, *Nat. Photonics*, 2017, **11**, 63–68.
19 A. Poloek, C. W. Lin, C.-T. Chen and C.-T. Chen, *J. Mater. Chem. C*, 2014, **2**, 10343–10356.
20 A. Poloek, C. Wang, Y. T. Chang, C. W. Lin, C.-T. Chen and C.-T. Chen, *J. Mater. Chem. C*, 2015, **3**, 11163–11177.
21 A. Poloek, C.-T. Chen and C.-T. Chen, *J. Mater. Chem. C*, 2014, **2**, 1376–1380.
22 S. Li, X. Li, Q. Li, Q. Yuan, X. Shi and Q. Xu, *Green Chem.*, 2015, **17**, 3260–3265.
23 S. Chen, G. Tan, W. Wong and H. Kwok, *Adv. Funct. Mater.*, 2011, **21**, 3785–3793.
24 Crystal data for **AtFOND**: $C_{27}H_{18}F_3N_3O_3Pt$: F_w = 684.53, orthorhombic, *Pbcn*, Z = 8, F(000) = 2640. Cell dimendions:

a = 7.0583(2) Å, b = 29.4421(9) Å, c = 21.6515(7) Å, α = 90°, β = 90°, γ = 90°, V = 4499.4(2) Å^3, 2θ max = 50.5°, r_{cacld} = 2.021 mg m^{-3}. Of 96 170 reflections, 4967 were independence, 335 parameters, $R(F_o)$ = 0.0193 (for reflections with $I > 2s(I)$), $R_w(F_o)$ = 0.0436 (for reflections with $I > 2s(I)$). The GoF on F^2 was equal 1.103. **AtFNND**: $C_{23}H_{19}F_3N_4OPt$: F_w = 635.51, triclinic, $P\bar{1}$, Z = 4, F(000) = 1224. Cell dimendions: a = 12.0617(16) Å, b = 13.1230(18) Å, c = 14.549(2) Å, α = 69.047(4)°, β = 78.618(4)°, γ = 74.686(4)°, V = 2060.6(5) Å^3, 2θ max = 50.5°, r_{cacld} = 2.049 mg m^{-3}. Of 79 065 reflections, 9091 were independence, 599 parameters, $R(F_o)$ = 0.0314 (for reflections with $I > 2s(I)$), $R_w(F_o)$ = 0.0551 (for reflections with $I > 2s(I)$). The GoF on F^2 was equal 1.030. **PBSNND**: $C_{23}H_{18}N_4OPtS$: F_w = 593.56, orthorhombic, *Pbca*, Z = 8, F(000) = 2288. Cell dimendions: a = 21.8970(5) Å, b = 7.1898(2) Å, c = 24.3791(5) Å, α = 90°, β = 90°, γ = 90°, V = 3838.12(16) Å^3, 2θ max = 50.5°, r_{cacld} = 2.054 mg m^{-3}. Of 60 913 reflections, 4223 were independence, 273 parameters, $R(F_o)$ = 0.0153 (for reflections with $I > 2s(I)$), $R_w(F_o)$ = 0.0360 (for reflections with $I > 2s(I)$). The GoF on F^2 was equal 1.054. CCDC 2009562 (**AtFOND**), 2009563 (**AtFNND**), and 2009796 (**PBSNND**).

25 M. S. Lowry, W. R. Hudson, R. A. Pascal and S. Bernhard, *J. Am. Chem. Soc.*, 2004, **126**, 14129–14135.
26 X. Yang, F. I. Wu, H. Haverinen, J. Li, C. H. Cheng and G. E. Jabbour, *J. Appl. Phys. Lett.*, 2011, **98**, 033302.
27 X. Yang and G. E. Jabbour, *J. Mater. Chem. C*, 2013, **1**, 4663–4666.
28 H. T. Kidanu and C.-T. Chen, *J. Mater. Chem. C*, 2021, **9**, 1410–1418.
29 K. Araki, L. Angnes and H. E. Toma, *Adv. Mater.*, 1995, **7**, 554–559.
30 G. M. Sheldrick, *SHELXL-97*, University of Gottingen, Germany, 1977.
31 L. J. Farrugia, *J. Appl. Crystallogr.*, 1999, **32**, 837–838.
32 P. J. Low, M. A. J. Paterson, D. S. Yufit, J. A. K. Howard, J. C. Cherryman, D. R. Tackley, R. Brook and B. Brown, *J. Mater. Chem.*, 2005, **15**, 2304–2315.
33 J. Shi, C. W. Tang and C. H. Chen, *US Pat.*, 5645948, 1997.
34 S. Barlow, T. V. Timofeeva, J. Li, S. R. Marder, K. Y. Suponitsky and J.-Y. Cho, *J. Organomet. Chem.*, 2005, **690**, 4090–4093.
35 J. A. Lowe, O. J. Stacey, P. N. Horton, S. J. Coles and S. J. A. Pope, *J. Organomet. Chem.*, 2016, **805**, 87–93.